Optical evidence of many-body effects in the zincblende $Al_xGa_{1-x}N$ alloy system

View the article online for updates and enhancements.

IOP ebooks™

Bringing together innovative digital publishing with leading authors from the global scientific community.

Start exploring the collection−download the first chapter of every title for free.

Optical evidence of many-body effects in the zincblende $Al_xGa_{1-x}N$ alloy system

Elias Baron[1] , **Martin Feneberg**[1] , **Rüdiger Goldhahn**[1] , **Michael Deppe**[2],
Fabian Tacken[2] **and Donat J As**[2]

[1] Institut für Physik, Otto-von-Guericke-Universität Magdeburg, Universitätsplatz 2, 39106 Magdeburg, Germany
[2] Department of Physics, University of Paderborn, Warburger Straße 100, 33098 Paderborn, Germany

E-mail: elias.baron@ovgu.de

CrossMark

Abstract

We present a quantitative description of the change in optical properties of zincblende aluminium-gallium-nitride thin films dependent on the free-carrier concentration due to band filling and renormalization effects. Free-electron concentrations above 10^{20} cm^{-3} in GaN are achieved by introducing germanium as a donor. Spectroscopic ellipsometry in the infrared and ultraviolet spectral range yields the dielectric function (DF). The plasmon contribution for the infrared part of the DF allows to determine the free-electron concentration all-optically. Furthermore, by utilizing the Kane model for the band structure of semiconductors near the Γ-point of the Brillouin zone as well as taking into account Burstein-Moss-shift and band-gap renormalization, measured transition energies are efficiently described.

Keywords: doped semiconductors, ellipsometry, cubic nitrides, kp method

1. Introduction

Wide band gap semiconductors are still in high demand for various applications, such as optoelectronic devices, water purification and chemical or biological sensing [1, 2]. Band gap engineering is very beneficial for such applications. For this reason, aluminium-gallium-nitride ($Al_xGa_{1-x}N$) is a promising candidate for fabricating such devices. By varying the Al-concentration x, the band gap ranges from $E_G^{GaN} \approx$ 3.2 eV [3–5] to $E_G^{AlN} \approx$ 6 eV [6–8].

In addition to the widely known and researched hexagonal wurtzite phase, the cubic zincblende phase of group III-nitrides increasingly attracts interest to possibly replace the wurtzite phase in certain applications. Reasons for this are some intriguing properties of the zincblende phase which are believed to be advantageous over the wurtzite nitrides, such

as the absence of spontaneous and piezoelectric polarization [9, 10] and the higher symmetry [11]. Although zincblende nitrides are metastable [12], there have been several breakthroughs in control and quality of the preparation of those materials in recent years [13–18].

On the other hand, for many applications doping is a necessary step to increase performance. In this case, technically most relevant are highly *n*-type doped materials. The highest free-electron concentrations in zincblende AlGaN and GaN are reached by substituting the standard donor silicon by germanium [19, 20]. However, high free-carrier concentrations have a considerable impact on the optical properties of a material. Since the Fermi energy is pushed high into the conduction band, the exact shape of the band as well as many-body effects have to be taken into account.

In the current paper, we report the experimental and analytical results of different cubic AlGaN thin films, deposited by molecular beam epitaxy on a 3C-SiC and Si substrate in (001) orientation. Spectroscopic ellipsometry measurements between 27 meV and 6.5 eV are employed to derive the dielectric function (DF). Parameters obtained from the DF like plasma frequency and transition energy are analyzed in the framework of Kane's **k·p** perturbation theory. Furthermore,

Table 1. Sample list containing growth properties as well as experimental and analytical results: Al-concentration x measured by HRXRD, germanium effusion cell temperature T_{Ge}, zb-AlGaN layer thickness d_{refl} measured by reflectometric interference spectroscopy, transition energy $E_{CV,UVSE}$ determined by ultraviolet spectroscopic ellipsometry, and optical free-carrier concentration n_{IRSE} analytically derived from infrared ellipsometry.

Sample	x	Doping	T_{Ge} (°C)	d_{refl} (nm)	$E_{CV,UVSE}$ (eV)	n_{IRSE} (cm^{-3})
A1	0.00	Ge	800	427	3.23	1.321×10^{19}
A2	0.09	–	–	484	3.45	–
A3	0.10	Ge	800	480	3.47	1.263×10^{19}
A4	0.23	–	–	487	3.75	–
A5	0.26	Ge	800	456	3.79	7.124×10^{18}
A6	0.37	–	–	430	3.96	–
A7	0.38	Ge	800	336	4.14	5.835×10^{18}
A8	0.46	–	–	200	4.32	–
A9	0.48	Ge	800	160	4.39	6.907×10^{18}
A10	0.59	–	–	150	4.54	–
A11	1.00	–	–	~100	5.99	–
B1	0.23	–	–	497	3.73	–
B2	0.23	Ge	700	455	3.74	1.172×10^{19}
B3	0.27	Ge	800	437	3.87	3.097×10^{19}
B4	0.24	Ge	850	409	4.07	8.679×10^{19}
B5	0.22	Ge	900	438	4.27	1.440×10^{20}
B6	0.24	Ge	950	475	4.09	7.020×10^{19}

many-body effects like Burstein-Moss-shift and band gap renormalization (BGR) influencing the optical properties are included as well.

2. Experimental

For this study, cubic zincblende AlGaN (zb-AlGaN) samples grown on a 3C-SiC/Si substrate in (001) orientation by plasma-assisted molecular beam epitaxy are used. Some samples are degenerately doped by Ge. The samples were previously investigated by high-resolution x-ray diffraction (HRXRD) and reflection measurements to determine the Al-concentration and the AlGaN-layer thickness, respectively. A more detailed description of this as well as the growth process and substrate properties can be found elsewhere [19–24]. Here, two different sample series are presented. The samples of series A were grown with different Al-concentrations, between ≈10% and ≈70%, while the samples of series B hold very similar Al-concentrations of ≈25%, but offer different doping concentrations up to $n \approx 10^{20}$ cm^{-3} [21]. Furthermore, GaN and AlN reference samples are present in series A. All samples are listed in table 1, including some growth properties and experimental results.

The main experimental technique to investigate the optical properties of the samples was spectroscopic ellipsometry. Here, the infrared spectral region experiments were performed by a Woollam IR-VASE, based on Fourier-transform infrared spectroscopy, from 300 to 6000 cm^{-1} with a resolution of 4 cm^{-1}. A Woollam VASE (a scanning variable-angle spectroscopic ellipsometer based on a grating monochromator)

was employed in the range from 0.5 to 6.5 eV with a step size of 10 meV. Both instruments have overlapping spectral ranges. The angles of incidence Φ for both spectral regions were chosen to be 50°, 60°, and 70°, respectively.

Spectroscopic ellipsometry yields the ellipsometric angles Ψ and Δ, which correspond to the change in amplitude and phase of the reflected light. On the other hand, Ψ and Δ yield the complex reflection coefficient ρ [25] which can be rewritten in form of the so-called pseudo-DF $\langle\varepsilon\rangle$:

$$\rho = \tan(\Psi)\,e^{i\Delta}$$
$$\langle\varepsilon\rangle = \sin^2(\Phi)\left(1 + \tan^2(\Phi)\left(\frac{1-\rho}{1+\rho}\right)^2\right). \quad (1)$$

The experimental results for Ψ and Δ were analyzed by a multi-layer stack model resembling the sample structure. In our case, the multi-layer model consisted of the zb-AlGaN layer, on top of the 3C-SiC and the Si layer. In the visible/ultraviolet spectral range, an additional topmost layer accounting for surface roughness was appended to the multi-layer stack. The surface roughness was approximated by a Bruggeman effective medium approximation (50% void in zb-AlGaN matrix), modelling an effective DF from the two components [26]. A model containing phonon and plasmon contributions was used for the zb-AlGaN layer in the infrared region, further described in section 3.1. On the other hand, a so-called generalized oscillator model (GenOsc) containing different oscillators based on the Herzinger-Johs parameterized semiconductor oscillator functions (PSEMI) was used to describe the measured data in the visible and ultra-violet spectral region [27]. The parameters of zb-AlGaN layers' model were fitted to the experimental data of Ψ and Δ by numerically minimizing mean squared error values using a Levenberg-Marquardt algorithm. However, this is only the starting point for a point-by-point (pbp) fit which numerically changed the value of the DF wavelength-by-wavelength until the best agreement with the experimental data was achieved [28, 29]. The resulting pbp-DF is a necessary intermediate step for the analysis of the experimental pseudo-DF $\langle\varepsilon\rangle$ by the model DF ε. In the last step, we line-shape fitted the zb-AlGaN layer model (IR: phonon-plasmon, UV: GenOsc) again to the pbp-DF to obtain the most accurate values for the parameters of the DF, like phonon frequencies or transition energies.

3. Theory

In this section, we offer a description of the model DF in the infrared spectral region, which we use to analyze the experimental data, as well as the used band structure model for small values of k. Furthermore, an overview of the method to determine the free-carrier concentration, effective mass, and the considered many-body effects is given.

3.1. Dielectric function

The analysis of our experimental data was performed by fitting a model DF to the pbp-DF, based on the data for Ψ

and Δ. The complex DF $\varepsilon(\omega) = \varepsilon_1(\omega) + i\varepsilon_2(\omega)$ describes the linear dielectric response of the materials. In the infrared spectral region, the DF is dominated by phonon and plasmon contributions, which express the lattice oscillations and response of free-carriers in the material, respectively [30]. Here, the phonon contribution is described by the Lorentz model with harmonic oscillators, while the plasmon contribution was characterized by the Drude model. The infrared DF can thus be written as

$$\varepsilon(\omega) = \varepsilon_\infty + \sum_l \frac{S_l \omega_{\mathrm{TO}l}^2}{\omega_{\mathrm{TO}l}^2 - \omega^2 - i\gamma_{\mathrm{TO}l}\omega} - \frac{\omega_{\mathrm{P}}^2}{\omega^2 + i\gamma_{\mathrm{P}}\omega}, \quad (2)$$

with

$$\omega_{\mathrm{P}}^2 = \frac{e^2 n}{\varepsilon_0 m_{\mathrm{opt}}^*}. \quad (3)$$

Here, ε_∞ is the dielectric limit representing contributions from higher energy oscillators. Since zb-AlGaN is a ternary alloy semiconductor, we assume the phonon contribution to be a sum of more than one transverse-optical (TO) phonon. The parameters of the l-th TO phonon contribution consist of the amplitude S_l, the resonance frequency $\omega_{\mathrm{TO}l}$, and the broadening parameter $\gamma_{\mathrm{TO}l}$. The TO phonon frequencies for zb-GaN and AlN are reported to be ≈ 552 cm^{-1} [31–34] and ≈ 650 cm^{-1} [35, 36] respectively. Furthermore, in zb-GaN, there exists a weaker structure at approximately ≈ 542 cm^{-1} which derives from the occurrence of anharmonic effects [31–34]. The Drude term consists of the plasma frequency ω_{P} and the plasma broadening parameter γ_{P}. The plasma frequency is especially interesting for the analysis of the free-carrier concentration n and the optical effective electron mass m_{opt}^* of the material as detailed in section 3.3.

3.2. Band structure model

We approximate the band structure near the Γ-point of the Brillouin zone by Kane's model based on the $\mathbf{k} \cdot \mathbf{p}$ perturbation theory [37]. Here, one conduction band and three valence bands (light hole, heavy hole, and split-off band) are considered. Furthermore, we assume a direct band gap at the zone centre, isotropic bands, and a scalar effective mass. In the case of negligible spin-orbit splitting of the valence bands ($\Delta_{\mathrm{so}} \ll E_{\mathrm{G}}$), the conduction band dispersion is given by

$$E_{\mathrm{C}}(k) = \frac{\hbar^2 k^2}{2m_{\mathrm{e}}} + \frac{1}{2}\left(E_{\mathrm{G}} + \sqrt{E_{\mathrm{G}}^2 + 4P^2 k^2}\right), \quad (4)$$

with the free-electron mass m_{e}, the band gap E_{G}, and the momentum matrix element P. In most cases an energy parameter E_{P} is defined which relates to P and can be determined by comparing with the effective mass at the Γ-point of the Brillouin zone for the undoped material (band mass, $m_0^*(\Gamma)$)

$$E_{\mathrm{P}} = \frac{2m_{\mathrm{e}}}{\hbar^2} P^2 = E_{\mathrm{G}}\left(\frac{m_{\mathrm{e}}}{m_0^*(\Gamma)} - 1\right). \quad (5)$$

The reported band masses of 0.19 m_{e} for zb-GaN and 0.30 m_{e} for zb-AlN yield the P parameters of 0.724 and 0.730 eVnm, respectively [38–40]. Since the values of P for GaN and AlN are very similar to each other, we assume a linear interpolation between the two for zb-AlGaN

$$P_{\mathrm{Al}_x\mathrm{Ga}_{1-x}\mathrm{N}} = (P_{\mathrm{AlN}} - P_{\mathrm{GaN}}) \cdot x + P_{\mathrm{GaN}}. \quad (6)$$

The band gap of $\mathrm{Al}_x\mathrm{Ga}_{1-x}\mathrm{N}$ is characterized by band gap bowing

$$E_{\mathrm{G}}^{\mathrm{AlGaN}} = x \cdot E_{\mathrm{G}}^{\mathrm{AlN}} + (1-x) \cdot E_{\mathrm{G}}^{\mathrm{GaN}} + x \cdot (x-1) \cdot b, \quad (7)$$

with the bowing parameter $b = 0.85$ eV [6, 41]. Furthermore, previous studies suggest a crossing point between the direct ($\Gamma_{\mathrm{v}} \to \Gamma_{\mathrm{c}}$) and indirect ($\Gamma_{\mathrm{v}} \to X_{\mathrm{c}}$) transition for an Al-concentration of $x = 0.71$. [6] Therefore, the model described in equation (4) is only valid for samples with Al-concentrations $x \leq 0.71$.

3.3. Optical effective electron mass

The plasma frequency ω_{P} given in equation (3) is depending on both the free-carrier concentration and the optical effective electron mass. Many studies attribute this effective mass to the Fermi-energy for degenerately doped materials due to the phase-space filling of the conduction band with electrons [42–44]. However, since the incident light interacts with all electrons of the conduction band, an averaging over all occupied conduction band states is necessary. This is described by the so-called optical effective electron mass m_{opt}^*. To obtain m_{opt}^*, we analyze the quotient n/m_{opt}^*, which originates from the description of the free-carrier concentration n [45, 46]

$$\frac{n}{m_{\mathrm{opt}}^*} = \int_0^\infty \frac{D(k)f_{\mathrm{e}}}{Vm^*(k)} d^3 k. \quad (8)$$

Here, $D(k)$ is the density of states, V the crystal volume, f_{e} the Fermi–Dirac distribution and $m^*(k)$ the k-dependent effective mass

$$m^*(k) = \frac{\hbar^2 k}{\partial E_{\mathrm{C}}/\partial k}$$

$$\frac{1}{m^*(k)} = \frac{1}{m_{\mathrm{e}}} + \frac{2P^2}{\hbar^2 \sqrt{E_{\mathrm{G}}^2 + 4P^2 k^2}}. \quad (9)$$

By approximating f_{e} as a step function and introducing the Fermi-vector $k_{\mathrm{F}} = \left(3\pi^2 n\right)^{\frac{1}{3}}$, we are able to obtain the quotient n/m_{opt}^* and therefore make the connection between the experimentally obtained plasma frequency and the free-carrier concentration

$$\omega_{\mathrm{P}}^2 = \frac{e^2 n}{\varepsilon_0 m_{\mathrm{opt}}^*} = \frac{e^2}{\hbar^2 \pi^2 \varepsilon_0}\left[\frac{\hbar^2 k_{\mathrm{F}}^3}{3m_{\mathrm{e}}} + \frac{1}{4}k_{\mathrm{F}}\sqrt{E_{\mathrm{G}}^2 + 4P^2 k_{\mathrm{F}}^2}\right.$$
$$\left. - \frac{E_{\mathrm{G}}^2}{8P}\ln\left(\frac{2Pk_{\mathrm{F}} + \sqrt{E_{\mathrm{G}}^2 + 4P^2 k_{\mathrm{F}}^2}}{E_{\mathrm{G}}}\right)\right]. \quad (10)$$

Table 2. Parameters of the dielectric function obtained by infrared ellipsometry as defined in section 3.1.

Sample	S^{GaN}	ω_{TO}^{GaN} (cm^{-1})	γ_{TO}^{GaN} (cm^{-1})	S^{anharm}	ω_{TO}^{anharm} (cm^{-1})	γ_{TO}^{anharm} (cm^{-1})	S^{AlN}	ω_{TO}^{AlN} (cm^{-1})	γ_{TO}^{AlN} (cm^{-1})	ω_{P} (cm^{-1})	γ_{P} (cm^{-1})
A1	2.94 ± 0.10	552 ± 0.05	7.42 ± 0.18	2.17 ± 0.12	543 ± 0.19	10.5 ± 0.56	—	—	—	2498 ± 101	101 ± 18.4
A2	2.84 ± 0.12	557 ± 0.07	7.42 ± 0.23	1.37 ± 0.13	549 ± 0.31	10.5 ± 0.69	—	—	—	—	—
A3	3.42 ± 0.04	558 ± 0.03	7.23 ± 0.08	0.37 ± 0.04	548 ± 0.34	7.83 ± 1.06	0.09 ± 0.02	638 ± 2.07	23.6 ± 3.02	2587 ± 23.2	819 ± 17.1
A4	3.38 ± 0.10	564 ± 0.12	12.4 ± 0.37	0.30 ± 0.06	554 ± 0.32	5.74 ± 1.12	0.64 ± 0.11	630 ± 2.86	46.2 ± 9.61	—	—
A5	2.69 ± 0.67	566 ± 0.73	14.5 ± 0.46	0.67 ± 0.64	561 ± 1.15	10.2 ± 2.61	0.71 ± 0.08	631 ± 1.56	50.1 ± 5.58	1725 ± 33.9	508 ± 58.8
A6	2.88 ± 0.29	572 ± 0.62	18.3 ± 0.84	0.27 ± 0.23	565 ± 0.79	7.64 ± 3.71	1.34 ± 0.12	626 ± 1.34	43.4 ± 4.60	—	—
A7	2.06 ± 0.41	575 ± 1.06	19.1 ± 1.13	0.96 ± 0.35	568 ± 0.45	10.4 ± 1.68	1.43 ± 0.09	631 ± 0.96	43.8 ± 3.23	1512 ± 34.9	304 ± 57.9
A8	1.84 ± 0.28	577 ± 0.35	14.1 ± 1.36	0.95 ± 0.41	593 ± 2.99	27.0 ± 8.37	1.48 ± 0.16	641 ± 1.21	36.2 ± 4.09	—	—
A9	1.88 ± 0.27	577 ± 0.34	14.3 ± 1.34	0.93 ± 0.41	594 ± 3.01	27.5 ± 8.08	1.46 ± 0.16	641 ± 1.21	35.9 ± 4.10	1619 ± 57.3	521 ± 50.2
A10	1.53 ± 0.34	578 ± 0.50	14.6 ± 1.89	0.95 ± 0.50	593 ± 3.33	26.7 ± 9.58	1.94 ± 2.18	641 ± 1.56	45.9 ± 4.98	—	—
A11	—	—	—	—	—	—	4.98 ± 0.13	651 ± 0.38	30.4 ± 1.09	—	—
B1	4.84 ± 1.10	560 ± 0.16	16.7 ± 0.49	—	—	—	0.91 ± 0.17	635 ± 3.16	43.1 ± 10.2	2110 ± 72.5	597 ± 65.3
B2	3.57 ± 0.03	564 ± 0.04	12.0 ± 0.14	—	—	—	0.82 ± 0.09	621 ± 2.18	62.2 ± 7.69	2224 ± 57.8	950 ± 65.0
B3	3.49 ± 0.04	565 ± 0.06	10.7 ± 0.18	—	—	—	1.13 ± 0.11	632 ± 2.36	72.2 ± 8.06	3582 ± 40.6	863 ± 24.1
B4	4.53 ± 0.06	566 ± 0.14	26.3 ± 0.46	—	—	—	0.97 ± 0.08	634 ± 1.49	48.0 ± 4.87	6283 ± 28.7	1390 ± 14.2
B5	4.96 ± 0.07	562 ± 0.21	35.1 ± 0.65	—	—	—	0.40 ± 0.08	639 ± 1.79	30.0 ± 5.52	7559 ± 20.7	1210 ± 7.44
B6	3.56 ± 0.05	568 ± 0.14	26.5 ± 0.48	—	—	—	0.98 ± 0.08	631 ± 1.55	56.9 ± 5.18	5297 ± 20.4	1125 ± 9.69

3.4. Many-body effects

In the preceding description, we considered the band gap E_G to be constant for a given Al-concentration. However, many-body effects have to be taken into account for a more accurate description. In this case, the BGR and Burstein-Moss shift (BMS) are the dominating effects [47–49]. Both have an increasingly strong effect on the optical properties with increasing free-carrier concentration. Therefore, they are especially important in degenerately doped material. The BGR describes a decreasing band gap due to electron-electron (ΔE_{ee}) and electron-ion (ΔE_{ei}) interactions. The renormalized band gap E_{ren} can be written as [30]

$$E_{ren}(n) = E_G - \Delta E_{BGR}(n), \qquad (11)$$

with

$$\Delta E_{BGR}(n) = \Delta E_{ee}(n) - \Delta E_{ei}(n). \qquad (12)$$

The interaction contributions are approximated by [49]

$$\Delta E_{ee}(n) = \frac{e^2 k_F}{2\pi^2 \varepsilon_0 \varepsilon_s} + \frac{e^2 k_{TF}}{8\pi \varepsilon_0 \varepsilon_s} \left[1 - \frac{4}{\pi} \arctan\left(\frac{k_F}{k_{TF}}\right) \right]$$

and

$$\Delta E_{ei}(n) = \frac{e^2 n}{\varepsilon_0 \varepsilon_s a_B k_{TF}^3}. \qquad (13)$$

Here, k_{TF} and a_B are the Thomas-Fermi screening vector and the effective Bohr-radius, respectively. Their calculation can be found elsewhere [31]. Furthermore, the static dielectric constant $\varepsilon_s = \lim_{\omega \to 0}(\varepsilon_1)$ depends on the material. Once more, a linear interpolation for zb-AlGaN is assumed since the values of ε_s for zb-GaN (9.44) [3] and zb-AlN (8.71) [7] are very similar.

Consequently, E_{ren} replaces E_G in equation (4) and therefore in equations (9) and (10) as well. On the other hand, the phase-space filling of the conduction band with electrons yields an increase of the transition energy between the conduction band and the valence bands due to Pauli-blockage and k-conservation. The transition energy E_{CV} consists of a conduction and a valence band contribution, both at the Fermi-vector k_F

$$E_{BMS} = \Delta E_C + \Delta E_V = E_C(k_F) + |E_V(k_F)|. \qquad (14)$$

The conduction band contribution is simply the dispersion given in equation (4). For the valence bands, we approximate the more complicated dispersions by a single parabolic band with the averaged hole mass $\bar{m}_h$ as defined by

$$E_V(k) = -\frac{\hbar^2 k^2}{2\bar{m}_h}. \qquad (15)$$

The transition energy is consequently written as

$$E_{CV} = \frac{\hbar^2 k_F^2}{2}\left(\frac{1}{m_e} + \frac{1}{\bar{m}_h}\right) + \frac{1}{2}\left(E_{ren} + \sqrt{E_{ren}^2 + 4P^2 k_F^2}\right). \qquad (16)$$
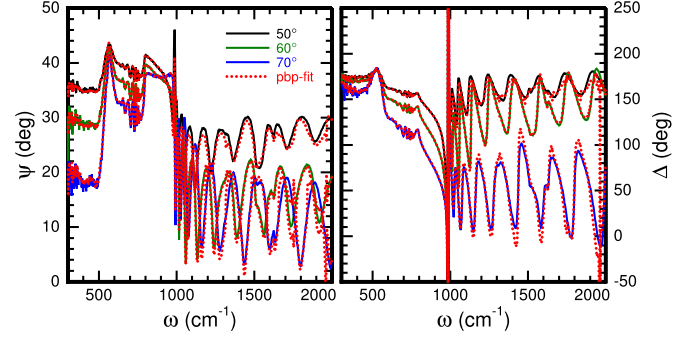

Figure 1. Ellipsometric angles Ψ and Δ and the corresponding point-by-point-fit (pbp-fit, red dotted curves) of sample A3 ($x = 0.10$, $n_{IRSE} = 1.26 \times 10^{19}$ cm^{-3}) in the infrared range measured by spectroscopic ellipsometry for three angles of incidence.

4. Results and discussion

Our experimental and analysis results are presented in this part, both for the infrared and visible/ultra-violet spectral regions. The analysis is based on the models described in section 3. Furthermore, an investigation on the observed phonon frequencies is performed.

4.1. Infrared spectroscopic ellipsometry

Infrared spectroscopic ellipsometry (IRSE) was performed on all samples and the resulting experimental data analyzed by the model described in section 3.1. Here, we focus on three selected samples as examples to discuss the differences occurring due to Al-concentration and doping levels. Nevertheless, the phonon and plasmon parameters for the DF of all samples are shown in table 2.

First, we look at sample A3 as a reference for low doping and low Al-concentration. The experimental data (Ψ and Δ) as well as the pbp-fit are shown in figure 1. A very good agreement is achieved for wavenumbers below 1000 cm^{-1}, where the TO phonon contributions are expected. The strong feature at $\approx$1000 cm^{-1} is attributed to the 3C-SiC substrate. For higher wavenumbers, the spectrum is dominated by Fabry-Pérot oscillations due to thin-film interference caused by the different interfaces.

The resulting pbp-DF of the zb-AlGaN layer is then used to determine the model DF described by equation (2), shown in figure 2. Here, the spectral region was reduced for clarity since there are no features of the zb-AlGaN layer above 1000 cm^{-1}. Again, a good fit result was achieved. A strong phonon contribution is clearly visible at $\approx$558 cm^{-1}, which consists of the GaN-like TO phonon and an anharmonic shoulder as described in section 3.1 (see inset in figure 2). The values of the resonance frequencies are slightly shifted to higher wavenumbers compared to binary GaN. On top of that, the plasmon contribution is best visible as an increase of the imaginary part ε_2 of the DF.

As a second example we look at sample A9, which is characterized by a higher Al-concentration ($x = 0.48$) than sample A3. The experimental data (Ψ and Δ) are shown in figure 3,
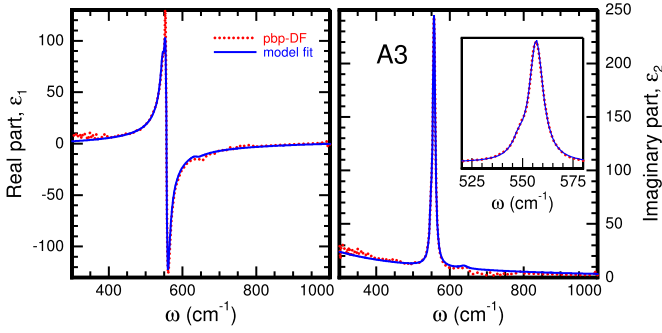
Figure 2. Point-by-point fitted (pbp-DF, dotted) and analytical model (model fit, continuous) dielectric function for sample A3 ($x = 0.10$, $n_{IRSE} = 1.26 \times 10^{19}$ cm^{-3}) in the infrared range. The inset on the right side displays a magnified spectral region of the GaN phonon contribution to indicate the anharmonic shoulder.
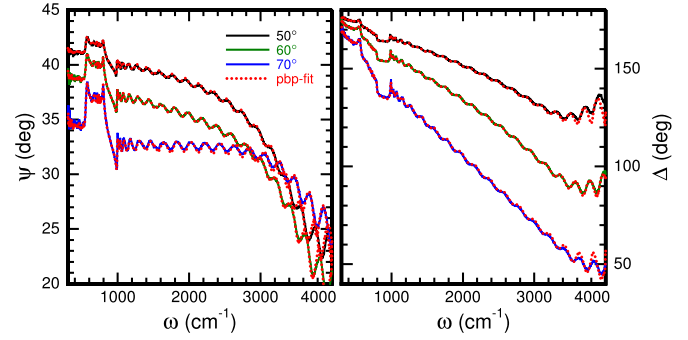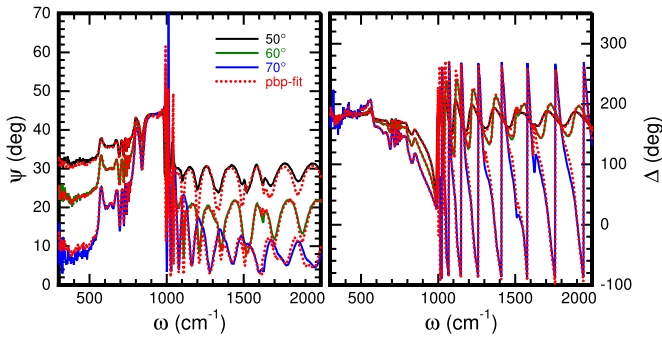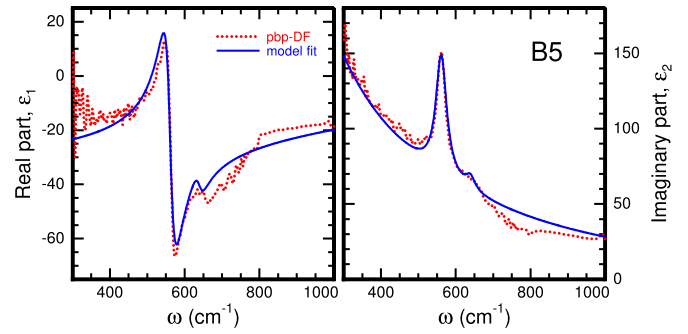

Figure 3. Ellipsometric angles Ψ and Δ and the corresponding point-by-point-fit (pbp-fit, red dotted curves) of sample A9 ($x = 0.48$, $n_{IRSE} = 6.91 \times 10^{18}$ cm^{-3}) in the infrared range measured by spectroscopic ellipsometry for three angles of incidence.
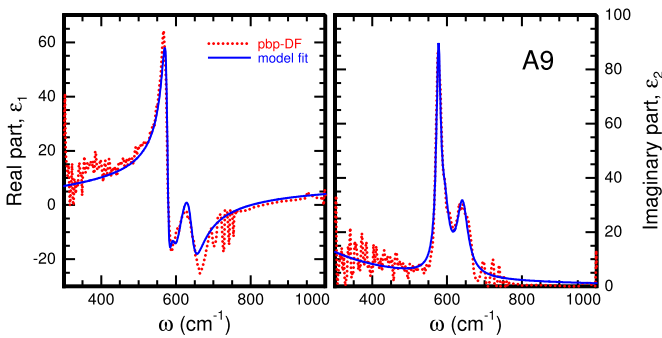

Figure 4. Point-by-point fitted (pbp, dotted) and analytical model (model fit, continuous) dielectric function for sample A9 ($x = 0.48$, $n_{IRSE} = 6.91 \times 10^{18}$ cm^{-3}) in the infrared range.

where the higher wavenumbers are again dominated by Fabry-Pérot oscillations. However, the DF in figure 4 is dominated by two distinct phonon modes in striking difference to the case of sample A3 (figure 2). In agreement with the literature [36, 50], we attribute the stronger one as GaN-like and the weaker one as AlN-like. Both resonance frequencies vary from the corresponding GaN or AlN values due to the ternary nature of the material.

Figure 5. Ellipsometric angles Ψ and Δ and the corresponding point-by-point-fit (pbp-fit, red dotted curves) of sample B5 ($x = 0.22$, $n_{IRSE} = 1.44 \times 10^{20}$ cm^{-3}) in the infrared range measured by spectroscopic ellipsometry for three angles of incidence.

Figure 6. Point-by-point fitted (pbp, dotted) and analytical model (model fit, continuous) dielectric function for sample B5 ($x = 0.22$, $n_{IRSE} = 1.44 \times 10^{20}$ cm^{-3}) in the infrared range.

Finally, we take a look at the degenerately doped sample B5 ($x = 0.22$). Again, the experimental data (Ψ and Δ) as well as the model DF are shown in figures 5 and 6, respectively. A drastic difference in the spectra (Ψ and Δ) compared to the lower doped samples of series A is observed. While the Fabry-Pérot oscillations above 1000 cm^{-1} are still present, they are damped compared to figures 1 and 3. Furthermore, the values of Ψ and Δ are steeply decreasing for higher wavenumbers. We want to emphasize that this is not just due to the increased wavenumber region shown in figure 5. The plasmon contribution is much more dominant than in figures 2 or 4 , which indicates a higher free-carrier concentration in this sample. In addition, the two phonon contributions of the stronger GaN-like phonon and weaker AlN-like phonon from before are observed again. However, in this case, we do not detect the anharmonic shoulder like for the other samples. Differences between the pbp- and the model DF in figure 6 are very likely due to data noise.

The imaginary parts of the DFs of all samples from series A and B are shown for comparison in figures 7 and 8. First, we look at the influence of different Al-concentrations on the phonon contributions for samples of series A. A shift of the GaN-like TO phonon frequency from 550 cm^{-1} up to nearly 590 cm^{-1} is very pronounced with increasing Al-concentration, while the shift of the AlN-like TO phonon is less noticeable due to the smaller amplitude, but still clearly
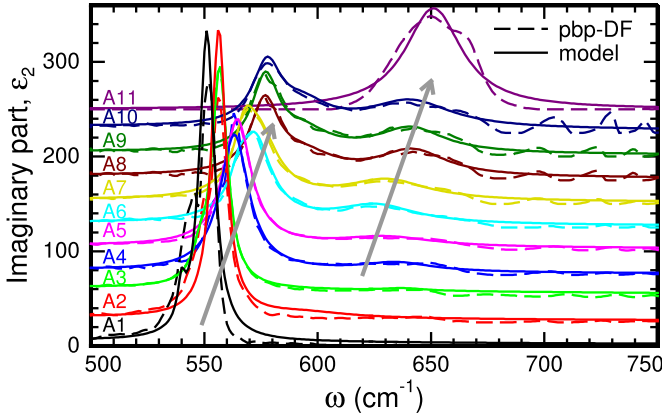
J. Phys. D: Appl. Phys. **54** (2021) 025101

E Baron *et al*

Figure 7. Point-by-point fitted (pbp-DF, dashed) imaginary parts of all A series samples as well as the corresponding analytical line shape fits (model, continuous). A vertical shift between each curve is artificially implemented for better visibility. Arrows indicate the resonant frequency shifts with increasing Al-concentration.
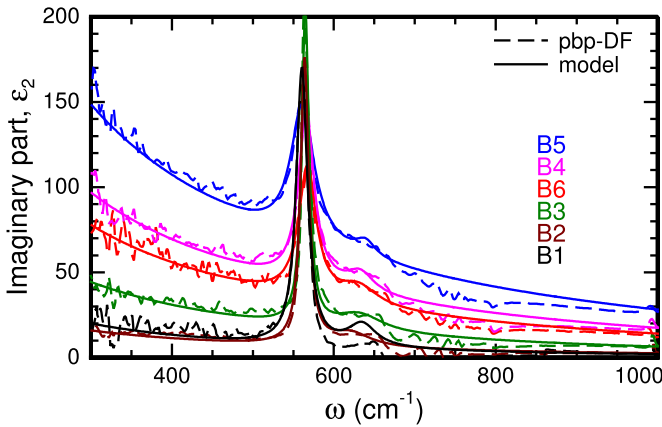

Figure 8. Point-by-point fitted (pbp-DF, dashed) imaginary partsof all B series samples as well as the corresponding analytical line shape fits (model, continuous). The observed amplitude shift for lower wavenumbers originates from the different plasmon contributions.

Figure 9. Transverse optical phonon frequencies ω_{TO} and amplitudes S of all samples according to equation (2). Error bars represent the broadening parameters γ_{TO}. The AlN-like (red) and the two GaN-like (blue, green) phonon modes show an approximately linear dependence on the Al-concentration x.

AlN-like modes are much broader, an increasing energy position with increasing Al-concentration is detectable, approaching the AlN TO phonon frequency as expected. It should be noted, that the broadening parameters of series B are consistently higher than those of series A. Furthermore, the amplitude behaviour displays a distinct transfer from the GaN-like mode to the AlN-like mode with increasing Al-concentration. In fact, at $x \approx 0.50$ the amplitudes have very similar values. The amplitude of the anharmonic shoulder of the GaN-like mode varies strongly for Al-concentration below 25%, but is found to be constant for Al-concentrations above 25%.

In the next step, we extract the plasma frequencies from the model DF described in section 3.1. We present the relation between the plasma frequency ω_{P} and the free-carrier concentration n for three different Al-concentrations x in figure 10 by utilizing equation (10). The small difference in P defined in equation (6) only yields a negligible change of ω_{P}. The intersection of the experimentally obtained plasma frequencies and equation (6) yields the optical free-carrier concentration n_{IRSE}.

The optically obtained free-carrier concentration n_{IRSE} enables us to determine the effective electron masses. This is exemplary shown in figure 11 for three samples. Here, the increasing band mass m_0^* due to the increasing Al-concentration is clearly visible. Furthermore, the included renormalization effects initially cause a slight decrease of the effective masses (see inset of figure 11) until the conduction band filling becomes predominant.

4.2. Ultraviolet spectroscopic ellipsometry

The experimental data and the pbp-fit of sample A3 measured by ultraviolet spectroscopic ellipsometry (UVSE) are shown in figure 12 . Here, Fabry-Pérot oscillations are visible at lower energies connecting to the infrared spectral region in figure 1. The oscillations disappear in the vicinity of the absorption edge. The related pbp-DF is displayed in figure 13.

The transition energy $E_{\text{CV,UVSE}}$ (as marked by vertical arrows in figures 13 and 15) between the conduction and valence bands is determined by a line-shape fit of the Gen-Osc model to the pbp-DF. A so-called PSEMI-0 oscillator [27] was used within the GenOsc model to represent the

present. Furthermore, a transfer of oscillator strength from the GaN-like phonon to the AlN-phonon is observed, which is attributed to the increasing AlN fraction. On the other hand, the different amplitudes of the imaginary parts for lower wavenumbers in the Drude contribution in figure 8 indicate different free-carrier concentrations in the corresponding samples of the B series, while the phonon energy position remains stable due to the similar Al-concentrations of $x \approx 0.25$.

For further analysis, we extract the parameters described in section 3.1 from the experimentally obtained model DFs, especially the phonon parameters and the plasma frequency. First, the TO phonon frequencies and amplitudes are collected in figure 9. There, a seemingly linear shift to higher wavenumbers with increasing Al-concentration is obvious for the GaN-like mode and the anharmonic shoulder. Although the
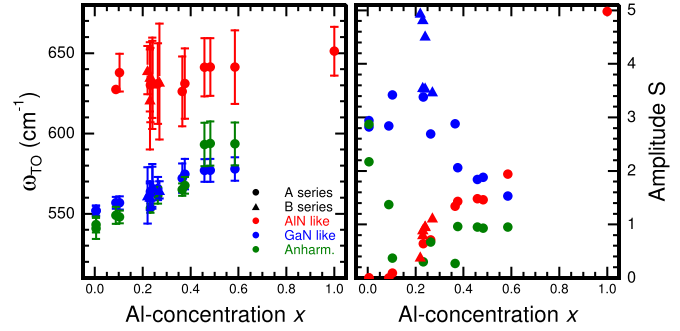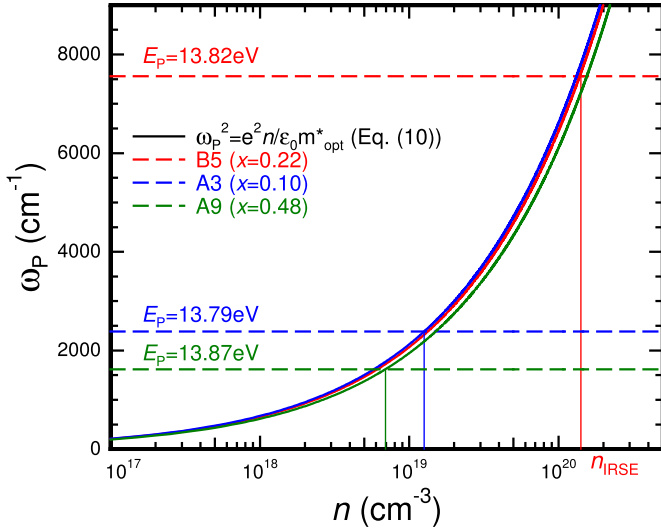
J. Phys. D: Appl. Phys. **54** (2021) 025101

E Baron *et al*

Figure 10. Plasma frequencies ω_P calculated by equation (10) (continuous lines) including band gap renormalization effects and the experimentally obtained plasma frequencies for different samples (dashed lines). The intersection of these lines determines the optical free-carrier concentration n_{IRSE}.
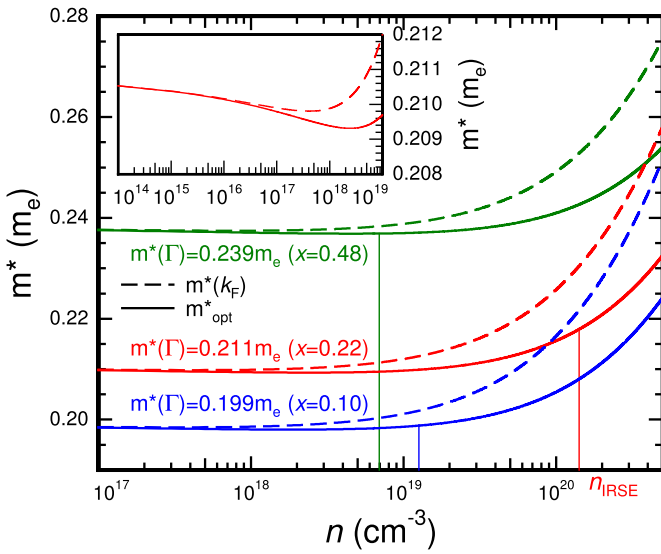

Figure 11. Effective mass at the Fermi-vector ($m^*(k_F)$, dashed) and optical effective mass (m^*_{opt}, continuous) for three different Al-concentrations (red, blue, and green) as a function of free-carrier concentration. Band gap renormalization effects induce an initial decrease of the effective masses (see inset). The increase of the optical effective mass due to the then predominant band filling effects, for instance for an Al-concentration of $x = 0.22$, starts for $n \approx 2 \times 10^{18}$ cm^{-3}. The optical free-carrier concentration n_{IRSE} yields the marked effective masses.

Figure 12. Ellipsometric angles Ψ and Δ and the corresponding point-by-point-fit (pbp-fit, red dotted curves) of sample A3 ($x = 0.10$, $n_{IRSE} = 1.26 \times 10^{19}$ cm^{-3}) in the visible/ultraviolet range measured by spectroscopic ellipsometry for three angles of incidence.

Figure 13. Point-by-point fitted dielectric function (pbp-DF, dotted) and line-shape fit (continuous) for sample A3 ($x = 0.10$, $n_{IRSE} = 1.26 \times 10^{19}$ cm^{-3}) with a transition energy of ≈ 3.47 eV.

Figure 14. Ellipsometric angles Ψ and Δ and the corresponding point-by-point-fit (pbp-fit, red dotted curves) of sample B5 ($x = 0.22$, $n_{IRSE} = 1.44 \times 10^{20}$ cm^{-3}) in the visible/ultraviolet range measured by spectroscopic ellipsometry for three angles of incidence.

general line-shape of ε_2 around the absorption onset, which resembles a Fermi–Dirac distribution. The critical point of the PSEMI-0 oscillator corresponds to the inflection point of the curve which coincides with the transition energy. For example, the spectrum shown in figure 13 yields a transition energy of ≈ 3.47 eV. Similar experimental results can be found for sample B5 in figures 14 and 15. Here, Fabry-Pérot oscillations
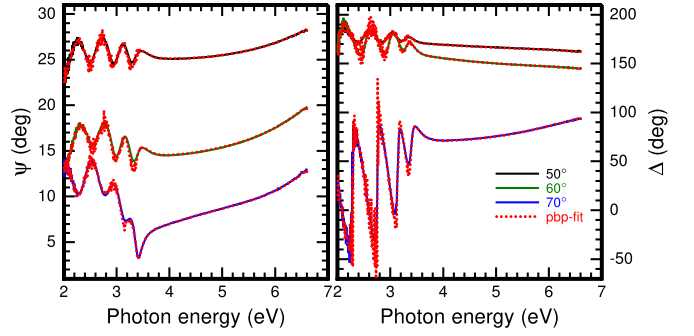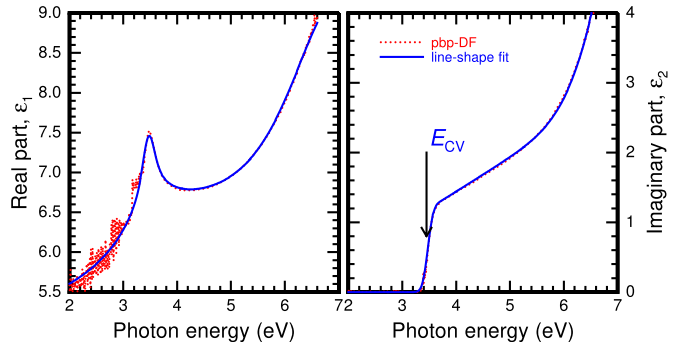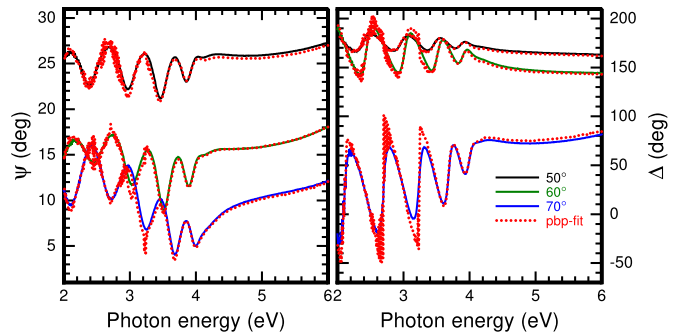
are once more visible until the absorption edge. Due to the higher Al- and free-electron concentration, the band edge in ε_2 displays a broader line shape with a higher transition energy of ≈ 4.27 eV. Please note that irregularities below the absorption edge are residuals from the pbp-fit, most-likely due to the Fabry-Pérot oscillations. This also applies for ε_1 in figure 13.

The imaginary parts of all A series samples are shown in figure 16. Here, a blue shift of the transition energy is observed

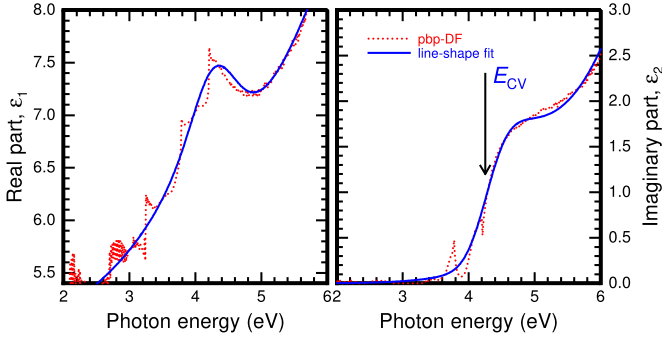J. Phys. D: Appl. Phys. **54** (2021) 025101

E Baron *et al*

Figure 15. Point-by-point fitted dielectric function (pbp-DF, dotted) and line-shape fit (continuous) for sample B5 ($x = 0.22$, $n_{IRSE} = 1.44 \times 10^{20}$ cm^{-3}) with a transition energy of ≈ 4.27 eV.

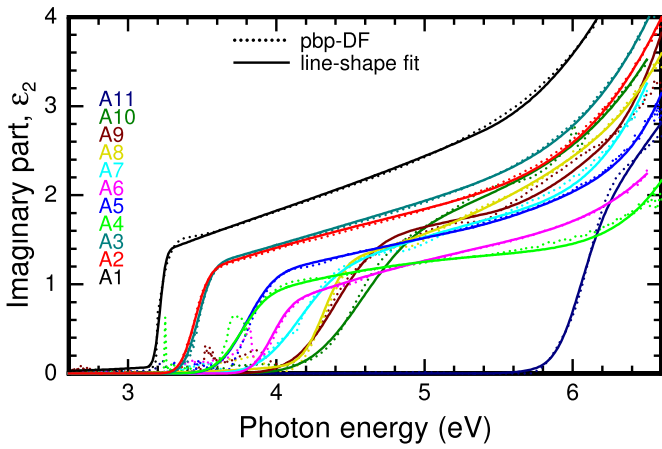**Figure 16.** Point-by-point fitted imaginary parts (pbp-DF, dotted) and line-shape fit (continuous) of all samples from series A.

Figure 17. Point-by-point fitted imaginary parts (pbp-DF, dotted) and line-shape fit (continuous) of all samples from series B.

Figure 18. Experimentally obtained transition energies (symbols) as well as the behaviour of direct and indirect band gaps [6] (dashed lines).

with increasing Al-concentration. Since all series A samples have low doping, this shift is mostly due to the band gap bowing described in equation (7). On the other hand, imaginary parts of series B samples with very different doping levels but similar Al-concentrations are shown in figure 17. Here, we observe an increase of the transition energy as well. However, in this case the blue shift is primarily a result of the phase-space filling of the conduction band, the so-called BMS as described in section 3.4.

The experimentally obtained transition energies of all samples are plotted as a function of the Al-concentration in figure 18. Here, the band-gap bowing as well as the indirect band gap are shown for comparison [6]. The A series' transition energies are in good agreement with the band-gap bowing curve. Small variations from the theoretical curve could indicate the effect of BGR and BMS. The transition energy, much like the effective mass, actually decreases for low free-carrier concentration ($n \leq 10^{18}$ cm^{-3}) due to BGR, before an equilibrium between BGR and BMS is reached (see inset of figure 11). This assumption, however, can not satisfyingly be confirmed, since most of the A series' samples do not show significant plasmon contributions in their IR data. On the other hand, the B series' transition energies are located at much
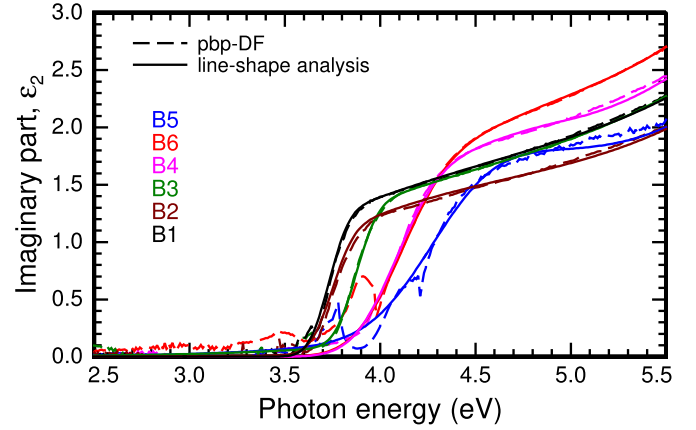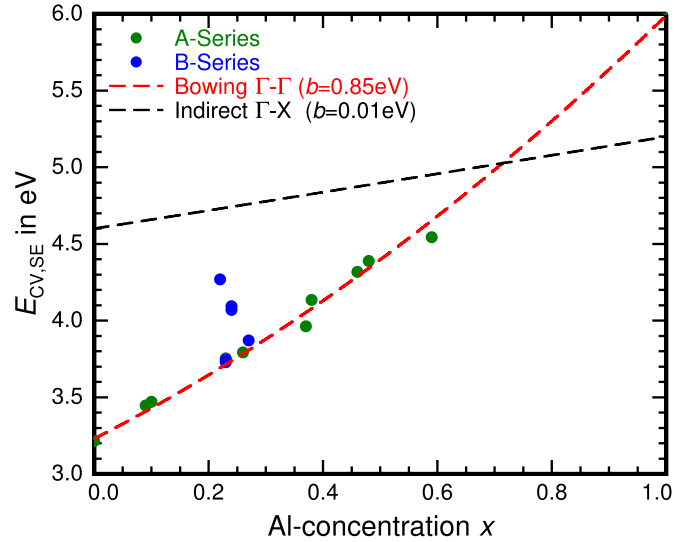
higher energies than the bowing curve, which definitely indicates a strong Burstein-Moss-shift due to high free-electron concentrations in those samples.

However, it turns out that the measured transition energies for samples of the B series do not comply with the free-electron concentrations determined by infrared spectroscopic ellipsometry n_{IRSE}. For example, to obtain a transition energy of 4.27 eV with an Al-concentration of 0.22 (see sample B5) a free-electron concentration of nearly 4×10^{20} cm^{-3} would be necessary, which is higher than $n_{IRSE} = 1.44 \times 10^{20}$ cm^{-3}. For this reason, we optimized our layer model described in section 2. We replaced the AlGaN layer by two differently high doped layers to explain our spectra. The topmost layer is very thin (e.g. ≈ 33 nm in B4) and represents a high doping layer, while a thicker layer for low doping concentrations continues. The overall AlGaN thickness remains nearly unchanged. This double-layer approach is motivated by experimental results found by Deppe *et al* for Ge doped cubic GaN
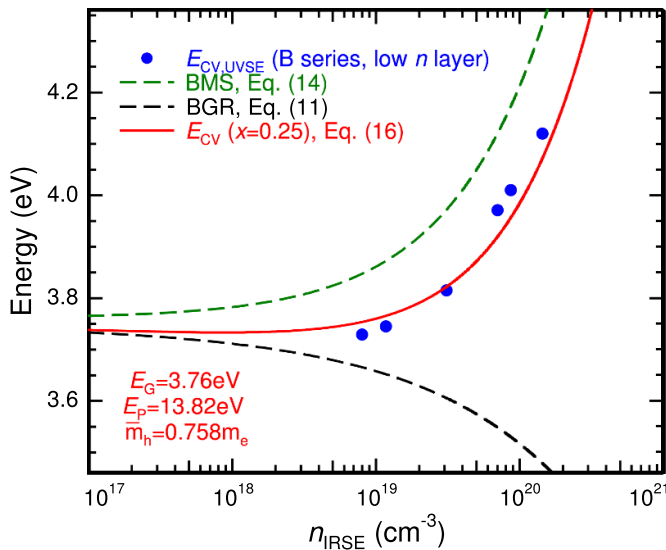
J. Phys. D: Appl. Phys. **54** (2021) 025101

E Baron *et al*

Figure 19. Experimentally obtained transition energies $E_{CV,UVSE}$ for the low doping zb-AlGaN layer (symbols) plotted as a function of the optical free-carrier concentration obtained by IRSE. The individual effects of Burstein-Moss shift (BMS, green dashed line) and band gap renormalization (BGR, black dashed line) are separately plotted as as well. The resulting model transition energy (continuous, red) resembles an Al-concentration of $x = 0.25$.

[19]. The modification leads to an improved model fit for Ψ and Δ and to the determination of two transition energies per sample. The transition energy for the lower doping concentration layer is in good agreement with n_{IRSE}. We conclude, that IRSE mainly measures the whole zb-AlGaN layer, while UVSE is more sensitive to individual sub-layers within the zb-AlGaN layer. This is expected, since the wavelength of UVSE is much shorter than IRSE.

The agreement of the model including many-body effects with the resulting transition energies is demonstrated in figure 19 for the low doped layer of the B series samples. Here, an Al-concentration of $x = 0.25$ was chosen for the determination of the model curves for BGR, BMS, and transition energy. Deviations between the model (red continuous curve) and measured (blue symbols) transition energies are mainly due to the deviations in the Al-concentration from $x = 0.25$ for each individual sample.

5. Summary

In conclusion, we determined the DFs of zb-AlGaN layers with Al-concentrations between 10% and 70% and doping levels up to 1.4×10^{20} cm^{-3} by spectroscopic ellipsometry from the infrared to the ultraviolet spectral range. Both, the energy position and the oscillator strength of the GaN- and AlN-like phonon contributions, display a nearly linear correlation with the Al-concentration. While the energy positions increase for both phonon modes, they exchange oscillator strengths from the GaN-like to the AlN-like for higher Al-content. The plasmon contribution is utilized to all-optically determine the free-carrier concentration and effective electron mass. By applying a two-layer AlGaN model for the

UVSE analysis, the experimentally obtained absorption edges are described by means of Burstein-Moss-shift and BGR. This is necessary due to the shorter wavelength of the UVSE which are able to detect finer layers with high doping concentrations, in comparison to the IRSE. Nevertheless, the agreement between absorption onsets and the applied model indisputably verifies the occurrence of many-body effects.

ORCID iDs

Elias Baron ⬤ https://orcid.org/0000-0002-8169-9372
Martin Feneberg ⬤ https://orcid.org/0000-0003-4253-0061
Rüdiger Goldhahn ⬤ https://orcid.org/0000-0001-8296-2331
Donat J As ⬤ https://orcid.org/0000-0003-1121-3565

References

[1] Chong M N, Jin B, Chow C W K and Saint C 2010 *Water Res.* **44** 2997
[2] Dasgupta P K, Li Q, Temkin H, Crawford M H, Fischer A J, Allerman A A, Bogart K H A and Lee S R 2004 *Proc. SPIE* **5530** 174
[3] Feneberg M *et al* 2012 *Phys. Rev. B* **85** 155207
[4] Lei T, Moustakas T D, Graham R J, He Y and Berkowitz S J 1992 *J. Appl. Phys.* **71** 4933
[5] Cervantes-Contreras M, López-López M, Meléndez-Lira M, Tamura M and Vidal M A 2003 *Thin Solid Films* **433** 68
[6] Landmann M *et al* 2013 *Phys. Rev. B* **87** 195210
[7] Röppischer M, Goldhahn R, Rossbach G, Schley P, Cobet C, Esser N, Schupp T, Lischka K and As D J 2009 *J. Appl. Phys.* **106** 076104
[8] Martinez-Guerrero E *et al* 2001 *Phys. Status Solidi* A **188** 695
[9] Li S F, Schörmann J, As D J and Lischka K 2007 *Appl. Phys. Lett.* **90** 071903
[10] Durniak M T, Bross A S, Elsaesser D, Chaudhuri A, Smith M L, Allerman A A, Lee S C, Brueck S R J and Wetzel C 2016 *Adv. Electron. Mater.* **2** 1500327
[11] Feneberg M, Winkler M, Lange K, Wieneke M, Witte H, Dadgar A and Goldhahn R 2018 *Appl. Phys. Express* **11** 101001
[12] Shi B M, Xi M H, Wu H S, Wang N and Tong S Y 2006 *Appl. Phys. Lett.* **89** 151921
[13] Cervantes-Contreras M, López-López M, Meléndez-Lira M, Tamura M and Hiroyama Y 2001 *J. Cryst. Growth* **227-228** 425
[14] Casallas-Moreno Y L *et al* 2015 *Appl. Surf. Sci.* **353** 588
[15] Lee L Y 2017 *Mat. Sci. Technol.* **33** 1570
[16] Liu R, Schaller R, Chen C Q and Bayram C 2018 *ACS Photonics* **5** 955
[17] Lee L Y, Frentrup M, Kappers M J, Oliver R A, Humphreys C J and Wallis D J 2018 *J. Appl. Phys.* **124** 105302
[18] Lozano J G, Morales F M, García R, González D, Lebedev V, Wang Ch Y, Cimalla V and Ambacher O 2007 *Appl. Phys. Lett.* **90** 091901

J. Phys. D: Appl. Phys. **54** (2021) 025101

E Baron *et al*

[19] Deppe M, Gerlach J W, Reuter D and As D J 2017 *Phys. Status Solidi* B **254** 1600700

[20] Deppe M, Gerlach J W, Shvarkov S, Rogalla D, Becker H-W, Reuter D and As D J 2019 *J. Appl. Phys.* **125** 095703

[21] Deppe M, Henksmeier T, Gerlach J W, Reuter D and As D J 2020 *Phys. Status Solidi* B **257** 1900532

[22] Costantini J-M, Miro S and Pluchery O 2017 *J. Phys. D: Appl. Phys.* **50** 095301

[23] Pezoldt J, Zgheib Ch, Lebedev V, Masri P and Ambacher O 2006 *Superlattices Microstruct.* **40** 612

[24] Scheiner J, Goldhahn R, Cimalla V, Ecke G, Attenberger W, Lindner J K M, Gobsch G and Pezoldt J 1999 *Mat. Sci. Eng.* B **61-62** 526

[25] Shokhovets S, Goldhahn R, Gobsch G, Piekh S, Lantier R, Rizzi A, Lebedev V and Richter W 2003 *J. Appl. Phys.* **94** 307

[26] Bruggeman D A G 1935 *Ann. Phys.* **24** 636

[27] Guide to Using WVASE Spectroscopic Ellipsometry Data Acquisition and Analysis Software 2012 Software manual, J.A. Woollam CO., Inc.

[28] Schmidt D and Schubert M 2013 *J. Appl. Phys.* **114** 083510

[29] Xie M-Y, Schubert M, Lu J, Persson P O A, Stanishev V, Hsiao C L, Chen L C, Schaff W J and Darakchieva V 2014 *Phys. Rev.* B **90** 195306

[30] Feneberg M, Nixdorf J, Lidig C, Goldhahn R, Galazka Z, Bierwagen O and Speck J S 2016 *Phys. Rev.* B **93** 045203

[31] Baron E, Goldhahn R, Deppe M, As D J and Feneberg M 2019 *Phys. Rev. Mat.* **3** 104603

[32] Mirjalili G, Parker T J, Shayesteh S F, Bülbül M M, Smith S R P, Cheng T S and Foxon C T 1998 *Phys. Rev.* B **57** 4656

[33] Lee S C, Ng S S, Abu Hassan H, Hassan Z, Zainal N, Novikov S V, Foxon C T and Kent A J 2014 *Mater. Chem. Phys.* **146** 121

[34] Cuscó R, Domènech-Amador N, Novikov S, Foxon C T and Artús L 2015 *Phys. Rev.* B **92** 075206

[35] Ibáñez J, Hernández S, Alarcón-Lladó E, Cuscó R, Artús L, Novikov S V, Foxon C T and Calleja E 2008 *J. Appl. Phys.* **104** 033544

[36] Harima H, Inoue T, Nakashima S, Okumura H, Ishida Y, Yoshida S, Koizumi T, Grille H and Bechstedt F 1999 *Appl. Phys. Lett.* **74** 191

[37] Kane E O 1957 *J. Phys. Chem. Solids* **1** 249

[38] Rinke P, Winkelnkemper M, Qteish A, Bimberg D, Neugebauer J and Scheffler M 2008 *Phys. Rev.* B **77** 075202

[39] de Carvalho L C, Schleife A and Bechstedt F 2011 *Phys. Rev.* B **84** 195105

[40] Kim K, Lambrecht W R L, Segall B and van Schilfgaarde M 1997 *Phys. Rev.* B **56** 7363

[41] Buchheim C, Goldhahn R, Rakel M, Cobet C, Esser N, Rossow U, Fuhrmann D and Hangleiter A 2005 *Phys. Status Solidi* B **242** 2610

[42] Schley P, Goldhahn R, Napierala C, Gobsch G, Schörmann J, As D J, Lischka K, Feneberg M and Thonke K 2008 *Semicond. Sci. Technol.* **23** 055001

[43] Feneberg M, Lange K, Lidig C, Wieneke M, Witte H, Bläsing J, Dadgar A, Krost A and Goldhahn R 2013 *Appl. Phys. Lett.* **103** 232104

[44] Schöche S, Kühne P, Hofmann T, Schubert M, Nilsson D, Kakanakova-Georgieva A, Janzén E and Darakchieva V 2013 *Appl. Phys. Lett.* **103** 212107

[45] Spitzer W G and Fan H Y 1957 *Phys. Rev.* **106** 882

[46] Hasselbeck M P and Enders P M 1998 *Phys. Rev.* B **57** 9674

[47] Moss T S 1954 *Proc. Phys. Soc.* B **67** 775

[48] Burstein E 1954 *Phys. Rev.* **93** 632

[49] Berggren K-F and Sernelius B E 1981 *Phys. Rev.* B **24** 1971

[50] Kasic A, Schubert M, Frey T, Köhler U, As D J and Herzinger C M 2002 *Phys. Rev.* B **65** 184302